

Article

A Simplified Treatment for Efficiently Modeling the Spectral Signal of Vibronic Transitions: Application to Aqueous Indole

Cheng Giuseppe Chen ¹, Massimiliano Aschi ², Marco D'Abramo ^{1,*} and Andrea Amadei ^{3,*}¹ Department of Chemistry, Sapienza University of Rome, 00185 Rome, Italy² Department of Chemical and Physical Sciences, University of L'Aquila, 67100 L'Aquila, Italy³ Department of Chemical and Technological Sciences, University of Tor Vergata, 00133 Rome, Italy

* Correspondence: marco.dabramo@uniroma1.it (M.D.); andrea.amadei@uniroma2.it (A.A.)

Abstract: In this paper, we introduce specific approximations to simplify the vibronic treatment in modeling absorption and emission spectra, allowing us to include a huge number of vibronic transitions in the calculations. Implementation of such a simplified vibronic treatment within our general approach for modelling vibronic spectra, based on molecular dynamics simulations and the perturbed matrix method, provided a quantitative reproduction of the absorption and emission spectra of aqueous indole with higher accuracy than the one obtained when using the existing vibronic treatment. Such results, showing the reliability of the approximations employed, indicate that the proposed method can be a very efficient and accurate tool for computational spectroscopy.

Keywords: indole; vibronic transitions; QM/MM; electronic states; theoretical chemistry; computational chemistry; absorption spectra; emission spectra



Citation: Chen, C.G.; Aschi, M.; D'Abramo, M.; Amadei, A.

A Simplified Treatment for Efficiently Modeling the Spectral Signal of Vibronic Transitions: Application to Aqueous Indole. *Molecules* **2022**, *27*, 8135. <https://doi.org/10.3390/molecules27238135>

Academic Editors: Magdalena Sałdyka and Maria Wierzejewska

Received: 27 October 2022

Accepted: 17 November 2022

Published: 22 November 2022

Publisher's Note: MDPI stays neutral with regard to jurisdictional claims in published maps and institutional affiliations.



Copyright: © 2022 by the authors. Licensee MDPI, Basel, Switzerland. This article is an open access article distributed under the terms and conditions of the Creative Commons Attribution (CC BY) license (<https://creativecommons.org/licenses/by/4.0/>).

1. Introduction

Tryptophan (Trp) fluorescence has long been applied to obtain structural and dynamical information about proteins. In fact, the extensively documented sensitivity of its spectroscopic properties to environment polarity makes Trp an attractive intrinsic probe in such systems [1–4]. This environment effect can be observed in both the wavelength and the intensity of its fluorescence spectrum, and it is generally accepted that the former reflects the degree of exposure to the solvent, ranging from λ_{max} of 308 nm in a very hydrophobic environment in azurin, to around 350 nm when completely exposed [1,4]. What still remains challenging is the possibility to interpret the spectral signal, beyond a simple qualitative assessment [5,6], providing detailed quantitative information on the molecular system of interest.

For such reasons, indole, the chromophore of the Trp amino acid, has been the subject of numerous experimental and theoretical studies [7–15]. Despite the relatively small size of the molecule, understanding its complex spectroscopic behavior requires accurately describing the electronic properties of its electronic ground and excited states (in particular for the excited states involving the first two gas-phase, i.e., unperturbed, spectroscopic active excited states named L_b and L_a) and to properly account for the vibrational structure of the corresponding electronic transitions (i.e., the vibronic transitions). The former aspect requires the use of computationally demanding methods [12], especially in order to identify the energy minimum of the L_a [9,10] excited state. At the same time, it is often not feasible to characterize all the relevant vibronic transitions (possibly a huge number) by means of the existing approaches [16,17], without using proper approximations resulting in a simplified efficient treatment. Finally, it is worth remarking on the need for an explicit (atomistic) solvent model and corresponding phase-space extended sampling to accurately reconstruct the effects of the perturbation on the chromophore spectral behavior, as further suggested by a very recent paper [15]. All these issues, i.e., high-level ab-initio calculations, explicit atomistic treatment of the solvent, an extended statistical sampling of the phase

space and the inclusion of all the relevant vibronic transitions, are crucial for a proper modelling of the vibronic spectra. Several efficient methods for reproducing vibronic spectra in condensed matter have appeared in the literature [17–22], as recently concisely and effectively reviewed in the work of Santoro et al. [17]. However, all such methods do not fully address all the above-mentioned important issues. In the present work, we further develop the approach presented in a previous work [23] for modelling vibronic spectra in condensed phase which was based on molecular dynamics (MD) simulations and the perturbed matrix method (PMM) [24–26] in combination with a widely used vibronic treatment [16]. The approach presented in this work, although maintaining the physical consistency of the theoretical–computational model, allows us to obtain rather accurate results even in the case of very complex systems, avoiding the use of highly expensive computational procedures. By employing the MD–PMM strategy and reasonable general approximations for treating the vibronic transitions, we model the environment perturbation effects on the chromophore quantum states, explicitly treating the dynamics of the atomistic water–chromophore interactions, and, hence, of the spectroscopic signal, over a much more extended statistical sampling of the system phase space (i.e., over a huge number of MD frames as obtained by a very extended MD simulation) and including a much larger number of vibronic transitions compared to the other methods. This is achieved by using, for each chromophore conformational basin (harmonic-like basin), the corresponding normal modes to provide the vibrational coordinates, assuming the quantum vibrational modes of different electronic eigenstates with similar frequencies to be identical, and, therefore, replacing the highly expensive integral calculations required to evaluate the vibrational eigenstate overlaps with the computation of undemanding single-mode integrals. In fact, similarly to the recently introduced approach of Santoro et al. [17], our approach allows us to distinguish between classical-like and quantum coordinate subspaces, permitting the use of only the quantum-mode transitions and, hence, of the minimum energy structures within the quantum internal coordinate subspace only, regardless of the positions of the semiclassical internal coordinates (e.g., at non-stationary points). However, in our approach, the use of the local full-space normal modes providing, within rather general and typically accurate approximations (see Appendix A), a proper definition of the quantum subspace (avoiding any a-priori possibly arbitrary choice) makes it possible to very easily separate and uncouple the corresponding vibronic transitions. Interestingly, such a feature of the method allows the use of the electronic state properly minimized reference configuration (e.g., by means of EOM-CCSD, necessary to obtain fully reliable results) still calculating the corresponding harmonic vibrational modes via a less accurate but computationally much more affordable method (e.g., TD-DFT). Note that the use of a lower level of theory for calculating the Hessian at the obtained higher level optimized geometry typically results in a few negative Hessian eigenvalues (i.e., the higher level optimized geometry is a saddle point for the lower level calculations), corresponding to a few classical-like modes (low-frequency modes). The efficiency of the proposed approach, which allows us to adopt expensive ab-initio calculations (in this case EOM-CCSD/6-311+G(d)) for obtaining the electronic properties and the minimized structures for each electronic state, accurately describe the perturbation effects over a very extended MD sampling and treat a huge number of vibronic transitions, made us confident about using this method to overcome the shortcomings that current strategies may incur (i.e., inaccurate perturbation treatment, insufficient phase space sampling, insufficient inclusion of vibronic transitions and inadequate description of the excited states [12]). The reported results show that the proposed extension of our MD–PMM approach, based on the use of the simplified vibronic treatment, can provide accurate predictions of both the absorption and fluorescence spectra of indole in aqueous solution, with a marked improvement compared to the results obtained using the previously employed vibronic treatment.

2. Theory

2.1. The Perturbed Vibronic Eigenstate

As usual for mixed quantum–classical models, we subdivide the system into the quantum center (QC), the subpart to be treated at quantum level, and the purely classical perturbing environment. The accurate evaluation of the QC electronic Hamiltonian operator (including the QC–environment interaction) and, hence, of the (perturbed) electronic eigenstates (electronic states) and properties can be used, in principle, to obtain any QC quantum process, possibly involving both the electronic and nuclear quantum degrees of freedom. It is worth noting that the QC nuclear semiclassical degrees of freedom, beyond the roto-translational coordinates, possibly include both the conformational coordinates corresponding to highly anharmonic degrees of freedom and providing large structural changes, and the semiclassical vibrational coordinates responsible, at each conformational configuration, for relatively small harmonic or quasi-harmonic structural fluctuations. Within the PMM framework, the electronic eigenstates are obtained by diagonalizing the electronic Hamiltonian at each QC–environment atomic configuration as (typically) given by MD simulations providing the position of the semiclassical coordinates, with the QC nuclear quantum degrees of freedom either at the corresponding energy-minimized position (when modelling electronic excitations and chemical reactions) or along predefined vibrational modes (when modeling vibrational excitations). Such MD–PMM calculations have been employed to evaluate, beyond the usual electronic spectra [27], the vibrational and vibronic equilibrium spectra [23,28–30], the electron-transfer thermodynamics and kinetics [31–34] and the time-resolved spectroscopic signals [35]. When modeling the vibronic transitions, we assume each vibronic eigenstate as properly described by the Born–Oppenheimer approximation and, hence, given within the coordinate representation by the combination of an electronic eigenstate Φ_i with a corresponding vibrational one $\phi_{i,m}$ (i.e., the m th vibrational eigenstate of the i th electronic eigenstate), providing the i, m vibronic eigenstate via their product $\Phi_i\phi_{i,m}$. Different levels of theory can be used to obtain the electronic eigenstates, based on the type of expansion/approximation used to express the perturbation operator within the electronic Hamiltonian [26]. A typically accurate approximation (used in this paper) for the Hamiltonian matrix \tilde{H}_e representing the electronic Hamiltonian operator \hat{H}_e within the unperturbed electronic eigenstate basis set Φ_j^0 (i.e., the eigenstates of the non-interacting QC) is [26]

$$\begin{aligned} [\tilde{H}_e]_{j,l} &= \langle \Phi_j^0 | \hat{H}_e | \Phi_l^0 \rangle \cong \left[\mathcal{U}_j^0 + \sum_N q_{N,j}^0 \mathcal{V}(\mathbf{R}_N) + \Delta V \right] \delta_{j,l} \\ &- \mathbf{E}(\mathbf{r}_0) \cdot \langle \Phi_j^0 | \hat{\boldsymbol{\mu}} | \Phi_l^0 \rangle (1 - \delta_{j,l}) \end{aligned} \quad (1)$$

where \mathcal{U}_j^0 is the energy of the j th unperturbed electronic eigenstate (i.e., the j th unperturbed electronic energy), N runs over the QC atoms with positions \mathbf{R}_N , $q_{N,j}^0$ is the N th atomic charge in the j th unperturbed eigenstate, $\mathcal{V}(\mathbf{R}_N)$ is the perturbing electric potential at the N th atom position, the scalar function ΔV (independent of the electronic states) approximates all the higher order terms of the diagonal elements, $\mathbf{E}(\mathbf{r}_0)$ is the perturbing electric field at the reference position \mathbf{r}_0 (typically the QC center of mass), and $\hat{\boldsymbol{\mu}}$ is the dipole operator and $\delta_{j,l}$ is the Kronecker delta. By means of the eigenvectors and eigenvalues of the Hamiltonian matrix provided by Equation (2), we can obtain any perturbed electronic property at each MD frame, and, in principle, the vibrational eigenstates and frequencies for each perturbed electronic eigenstate. Unfortunately, a complete evaluation of the perturbed vibrational eigenstates to be used when modeling vibronic spectra is computationally unfeasible and, thus, considering that the perturbed vibrational modes are typically virtually identical to the unperturbed ones [36] (i.e., to the vibrational modes of the unperturbed electronic eigenstate best corresponding to the perturbed electronic eigenstate) and the vibrational frequency variations due to the perturbation provide negligible changes in the excitation/relaxation energy of vibronic transitions involving an electronic excitation/relaxation, we can adopt

the approximation of using, for each perturbed electronic eigenstate, the unperturbed harmonic vibrational eigenstates and frequencies of the proper unperturbed electronic eigenstate (i.e., the unperturbed electronic eigenstate best matching the perturbed one) to reconstruct the (perturbed) vibronic eigenstates and related properties.

2.2. The Excitation and Emission Modeling

From the general expression providing the complete vibronic spectral signal [23], we obtain the extinction coefficient for a given (perturbed) excitation from the vibronic ground eigenstate to the m vibrational eigenstate of the i th electronic excited eigenstate (i.e., the $\Phi_0\phi_{0,0} \rightarrow \Phi_i\phi_{i,m}$ vibronic transition) with (perturbed) electronic transition dipole $\langle \Phi_0 | \hat{\mu} | \Phi_i \rangle = \mu_{0,i}$

$$\epsilon_{0,i}^m(\nu) \cong \sum_{\nu_{ref}^m} \frac{\Gamma_A(\nu_{ref}^m) n(\nu_{ref}^m) h\nu}{N_f} \frac{e^{-\frac{(\nu-\nu_{ref}^m)^2}{2\sigma^2}}}{\sigma\sqrt{2\pi}} \quad (2)$$

$$\Gamma_A(\nu_{ref}^m) = \frac{|\mu_{0,i}|_{\nu_{ref}^m}^2}{6\epsilon_0 c \hbar^2} |\langle \phi_{0,0}^0 | \phi_{j_i,m}^0 \rangle|_{\nu_{ref}^m}^2 \quad (3)$$

and the emission signal $k_{i,0}^m(\nu) \rho_m(\nu)$ (with $k_{i,0}^m(\nu)$ the emission rate constant and $\rho_m(\nu)$ the probability density of the emitting molecules) for the (perturbed) vibronic relaxation from the vibrational ground eigenstate of the i th electronic excited eigenstate to the m th vibrational eigenstate of the electronic ground eigenstate (i.e., for the $\Phi_i\phi_{i,0} \rightarrow \Phi_0\phi_{0,m}$ vibronic transition)

$$k_{i,0}^m(\nu) \rho_m(\nu) \cong \sum_{\nu_{ref}^m} \frac{\Gamma_E(\nu_{ref}^m) n(\nu_{ref}^m) (\nu/c)^3}{N_f} \frac{e^{-\frac{(\nu-\nu_{ref}^m)^2}{2\sigma^2}}}{\sigma\sqrt{2\pi}} \quad (4)$$

$$\Gamma_E(\nu_{ref}^m) = \frac{8\pi h |\mu_{0,i}|_{\nu_{ref}^m}^2}{6\epsilon_0 \hbar^2} |\langle \phi_{j_i,0}^0 | \phi_{0,m}^0 \rangle|_{\nu_{ref}^m}^2 \quad (5)$$

where c is the light speed, ϵ_0 is the vacuum dielectric constant, h is the Planck constant ($\hbar = h/(2\pi)$), the summation runs over the frequency bins used to construct the spectrum and identified by the m th vibronic transition reference frequencies ν_{ref}^m (i.e., the bin middle values), N_f is the total number of MD frames (necessarily a huge number to obtain a reliable spectral signal), $n(\nu_{ref}^m)$ is the number of MD frames with the m th vibronic transition frequency ν within the bin centered in ν_{ref}^m , and $|\mu_{0,i}|_{\nu_{ref}^m}^2$ is the corresponding electronic vertical transition dipole mean square norm as obtained averaging over the bin MD frames. Both the transition frequency and transition electronic dipole at each MD frame can be provided by the PMM using the MD frame semiclassical configuration to obtain the environment perturbation and QC atomic positions, relaxing only the QC vibrational quantum and semiclassical degrees of freedom at their energy-minimized positions [23,27], as given by the minimum energy structure of the unperturbed electronic ground eigenstate (Equations (2)–(3)) or the j_i unperturbed electronic eigenstate best corresponding at each frame to the i th perturbed electronic eigenstate (Equations (4)–(5)). Moreover, $|\langle \phi_{0,0}^0 | \phi_{j_i,m}^0 \rangle|_{\nu_{ref}^m}^2$ and $|\langle \phi_{j_i,0}^0 | \phi_{0,m}^0 \rangle|_{\nu_{ref}^m}^2$ are the mean square norms of the unperturbed vibrational eigenstate overlap, as obtained by averaging the bin frames possibly corresponding to different conformational basins, each providing different unperturbed properties. Furthermore, $\phi_{0,0}^0$ is the vibrational ground eigenstate of the unperturbed electronic ground eigenstate (typically virtually identical to the perturbed one), $\phi_{j_i,0}^0$ is the vibrational ground eigenstate of the unperturbed j_i electronic eigenstate, $\phi_{j_i,m}^0$ is the m th vibrational eigenstate of the j_i unperturbed electronic eigenstate, $\phi_{0,m}^0$ is the m th vibrational eigenstate of the unperturbed

electronic ground eigenstate and they are all modeled as harmonic vibrational eigenstates, each as obtained at the corresponding electronic eigenstate energy minimum for the vibrational coordinates. Note that for the excitation processes, the MD simulations used must correspond to the perturbed electronic ground eigenstate ensemble virtually identical to the unperturbed electronic eigenstate one, while for the relaxation processes the ensemble of the perturbed excited electronic eigenstate required is possibly not corresponding to a single unperturbed electronic eigenstate ensemble. Finally, the Gaussian distributions centered in ν_{ref}^m approximate, beyond the homogeneous broadening typically negligible in electronic excitations/relaxations, the broadening due to the QC semiclassical vibrations disregarded in PMM calculations, with the variance possibly estimated by a set of unperturbed electronic excitation energies corresponding to a set of QC configurations as obtained in principle by the MD sampling of the QC semiclassical vibrations [23] (note that, for sake of simplicity, we assume the same variance for all the Gaussian distributions).

In practice, for each electronic excitation by extracting the MD frames of the ground-state simulation with the i th perturbed electronic excited eigenstate best corresponding to a given j th unperturbed one and, for a flexible QC, also corresponding to a single conformation (MD sub-ensemble), we obtain the corresponding excitation vertical electronic spectrum by means of the electronic vertical energy and transition dipole, as provided by PMM [27], via

$$\varepsilon_{0,i}(\nu) \cong \sum_{\nu_{ref}} \frac{\Gamma_A(\nu_{ref})}{N_f} \frac{n(\nu_{ref})}{N_f} \frac{h\nu}{\sigma\sqrt{2\pi}} e^{-\frac{(\nu-\nu_{ref})^2}{2\sigma^2}} \quad (6)$$

$$\Gamma_A(\nu_{ref}) = \frac{|\mu_{0,i}|_{\nu_{ref}}^2}{6\epsilon_0 c \hbar^2} \quad (7)$$

with, now, the summation running over the frequency bins identified by the vertical electronic transition reference frequencies ν_{ref} , $n(\nu_{ref})$ the number of MD frames with the vertical electronic transition frequency ν within the bin centered in ν_{ref} and $|\mu_{0,i}|_{\nu_{ref}}^2$ the corresponding electronic vertical-transition dipole mean square norm as obtained by averaging over the bin MD frames. Note that by conformation we mean a configurational region of the internal semiclassical coordinate space (typically corresponding to a harmonic or quasi-harmonic basin) where all the QC electronic vertical-transition properties, except the vertical-transition energy, can be obtained at a single ground-state reference structure corresponding to a local energy minimum of the unperturbed electronic ground eigenstate (i.e., all such electronic properties are independent of the local configurational changes), considering the inherent fluctuations in the semiclassical internal coordinates as local classical vibrations. On the basis of the assumed negligible perturbation effects on the vibrational eigenstates and eigenvalues and noting that within a single sub-ensemble the unperturbed j_i electronic eigenstate is invariant and, hence, we can use the $j_i \rightarrow j$ substitution, we can reconstruct for each sub-ensemble the m th vibronic spectral peak by multiplying the vertical electronic spectrum by $|\langle \phi_{0,0}^0 | \phi_{j,m}^0 \rangle|^2$ (the square norm of the unperturbed vibrational eigenstate overlap in a single sub-ensemble, fully constant over those MD frames) and locating its maximum at

$$\nu_m = \nu_m^0 + \nu_{el} - \nu_{el}^0 \quad (8)$$

where ν_m^0 is the excitation frequency of the unperturbed m th vibronic transition (unperturbed m th vibronic frequency) possibly corrected to match the experimental gas-phase value, ν_{el} is the (perturbed) excitation frequency of the maximum of the electronic vertical spectrum and ν_{el}^0 is the excitation frequency of the unperturbed vertical electronic transition (unperturbed electronic vertical frequency). The sum of these vibronic peaks provides the sub-ensemble vibronic spectrum and, thus, summing such spectra over all the sub-ensembles, each statistically weighted by the corresponding probability as provided

by the ground state MD simulation, and then over all the relevant electronic excitations, we obtain the complete vibronic excitation spectrum. When dealing with electronic relaxations, a similar procedure is used, except that we utilize the excited-state MD simulation instead of the ground-state one to obtain the ensemble statistics, with the following expression

$$k_{i,0}(v) \rho(v) \cong \sum_{v_{ref}} \frac{\Gamma_E(v_{ref})}{N_f} \frac{n(v_{ref})}{N_f} \frac{(v/c)^3}{\sigma \sqrt{2\pi}} e^{-\frac{(v-v_{ref})^2}{2\sigma^2}} \quad (9)$$

$$\Gamma_E(v_{ref}) = \frac{8\pi h |\mu_{0,i}|_{v_{ref}}^2}{6\epsilon_0 \hbar^2} \quad (10)$$

providing for a given sub-ensemble the emission vertical electronic signal to be multiplied by $|\langle \phi_{j,0}^0 | \phi_{0,m}^0 \rangle|^2$, with now the electronic vertical transition frequency and transition dipole as obtained at the excited reference structure (i.e., the local energy minimum of the proper unperturbed electronic excited eigenstate). Moreover, we need for each electronic transition as many independent excited-state MD simulations as all the electronic conditions accessible to the perturbed excited eigenstate of interest, each well corresponding to a specific unperturbed electronic eigenstate providing the QC atomic charges and intramolecular properties to be used in the MD force field. Moreover, for each of such MD simulations, the sub-ensembles can only correspond to the different conformational conditions, as the final state of the emission is the electronic ground eigenstate virtually always well corresponding to the unperturbed electronic ground eigenstate (note that we need to remove from the excited-state simulation ensemble, if present, those configurations where the perturbed electronic excited eigenstate of interest is not coherent with the unperturbed one used to define the force field).

Finally, it is worth remarking that for each conformation of the ensemble MD simulation (the ground-state simulation for the excitation process and the excited-state simulation for the emission process), we use the corresponding ground- and excited-state reference structures, i.e., the energy minima of the unperturbed ground and excited electronic eigenstates, to obtain the unperturbed normal modes defining for each electronic eigenstate the QC quantum vibrational degrees of freedom via the modes with frequencies such that $h\nu > k_B T$ (k_B is the Boltzmann constant and T is the absolute temperature) and the QC semiclassical internal coordinates via all the other modes, except the roto-translational ones corresponding to the QC spatial changes due to the differential variations in the roto-translational coordinates (we always consider the roto-translational coordinates given by the center-of-mass Cartesian position and the Eulerian angles as semiclassical degrees of freedom). In the appendix, we discuss the conditions ensuring that such a choice provides for each conformation the proper definition of the internal coordinates.

2.3. A Simplified Efficient Strategy to Evaluate the Vibrational Overlap

From the previous theory subsections, it is evident that from the diagonalization of the perturbed electronic Hamiltonian matrix we can, in principle, obtain at each MD frame all the information necessary to reconstruct the spectroscopic signal according to Equations (6)–(10), once we have a proper estimate of $|\langle \phi_{0,0}^0 | \phi_{j,m}^0 \rangle|^2$ and $|\langle \phi_{j,0}^0 | \phi_{0,m}^0 \rangle|^2$ for each vibronic excitation and relaxation, respectively. However, the explicit evaluation of such vibrational eigenstate overlaps for the typically huge number of possibly significant vibronic transitions is computationally very demanding. Therefore, the available accurate methods for such calculations can be used for a limited number of vibronic peaks (a few hundred) and usually require for each electronic eigenstate the energy minimum in full configurational space [23,37]. Such restrictions can be overcome using proper approximations leading to a relevantly simplified procedure. In fact, when assuming for different electronic eigenstates, within each MD sub-ensemble, the corresponding quantum vibrational modes with approximately the same frequency being virtually identical, i.e., they are defined by the same mass-weighted Hessian eigenvector and, thus, share the same mode coordinate with

only different minimum energy positions, we can express the vibrational eigenstate overlaps via the product of the single-mode eigenstate overlaps $\langle \eta_{j,n,k}^0(\beta_n) | \eta_{j',n,k'}^0(\beta_n) \rangle$ where $\eta_{j,n,k}^0(\beta_n)$ and $\eta_{j',n,k'}^0(\beta_n)$ are the k and k' vibrational eigenstates of the n quantum mode, with coordinate β_n , for the j and j' electronic eigenstates, respectively. Note that within our assumption, $\eta_{j,n,k}^0(\beta_n)$ and $\eta_{j',n,k}^0(\beta_n)$ are identical except for the j and j' electronic eigenstate minimum-energy position along the mode coordinate β_n . Therefore, for the j, j' electronic eigenstate couple, the vibrational ground–ground overlap (i.e., the $m = 0$ vibronic transition) is

$$\langle \phi_{j,0}^0(\boldsymbol{\beta}) | \phi_{j',0}^0(\boldsymbol{\beta}) \rangle \cong \Pi_n \langle \eta_{j,n,0}^0(\beta_n) | \eta_{j',n,0}^0(\beta_n) \rangle \quad (11)$$

and for the m vibronic transition involving for the j' electronic eigenstate the k_m excited vibrational eigenstate of the n_m mode (i.e., single mode excitation), we have

$$\begin{aligned} \langle \phi_{j,0}^0(\boldsymbol{\beta}) | \phi_{j',m}^0(\boldsymbol{\beta}) \rangle &\cong \\ \langle \eta_{j,n_m,0}^0(\beta_{n_m}) | \eta_{j',n_m,k_m}^0(\beta_{n_m}) \rangle &\Pi_{n \neq n_m} \langle \eta_{j,n,0}^0(\beta_n) | \eta_{j',n,0}^0(\beta_n) \rangle \end{aligned} \quad (12)$$

with $\boldsymbol{\beta} = \{\beta_1, \beta_2, \dots, \beta_n, \dots\}$ the vector representing all the quantum-mode coordinates. When considering vibronic transitions involving multiple mode excitations for the j' electronic eigenstate (i.e., the $k_{m,l}$ excited vibrational eigenstates of the $n_{m,l}$ quantum modes with coordinates $\beta_{n_{m,l}}$), we have the general overlap expression

$$\begin{aligned} \langle \phi_{j,0}^0(\boldsymbol{\beta}) | \phi_{j',m}^0(\boldsymbol{\beta}) \rangle &\cong \\ \Pi_l \langle \eta_{j,n_{m,l},0}^0(\beta_{n_{m,l}}) | \eta_{j',n_{m,l},k_{m,l}}^0(\beta_{n_{m,l}}) \rangle &\Pi_{n \neq \mathbf{n}_m} \langle \eta_{j,n,0}^0(\beta_n) | \eta_{j',n,0}^0(\beta_n) \rangle \end{aligned} \quad (13)$$

with $\mathbf{n}_m = \{n_{m,1}, n_{m,2}, n_{m,3}, \dots, n_{m,l}, \dots\}$ the vector representing all the excited quantum modes. Finally, note that the vibrational eigenstates of any electronic state form a complete basis set for the vibrational state space, thus necessarily implying

$$\sum_m |\langle \phi_{j,0}^0 | \phi_{j',m}^0 \rangle|^2 = 1 \quad (14)$$

with m running over all the vibrational eigenstates of the unperturbed j' electronic state.

Equations (11)–(13) clearly show that within the approximation used, the evaluation of the vibrational overlap involving a very complex multiple integral is reduced to the product of single-mode integrals, each trivially evaluated using two harmonic vibrational wavefunctions corresponding to identical modes except for the minimum energy position along the shared mode coordinate. This approach can then allow us to include in the spectrum model a huge number of vibronic transitions, making straightforward the separation between the quantum vibrational coordinates and the semiclassical ones, thus possibly avoiding the restriction of using ground and excited reference structures strictly corresponding to full-space energy minima (we need only the quantum coordinates to be properly energy minimized).

3. Application to Aqueous Indole

3.1. Computational Details

The geometries of indole in the ground state and first three excited states were optimized in vacuum by means of CCSD and EOM-CCSD, using 6-311+G(d) as the basis set. The gas-phase electronic properties of the first six excited states were calculated for each geometry using EOM-CCSD, with 6-311+G(d) as the basis set. The harmonic vibrational eigenstates and frequencies were calculated by means of DFT and TD-DFT, with the functional M06-2X [38] and 6-311+G(d) as the basis set (the benchmarking [38–43] which resulted in this choice is described in detail in the Supplementary Materials; see Table S1 and Figure S1), using both the geometries optimized with the same level of theory (DFT) as

well as the geometries optimized with CCSD and EOM-CCSD. The geometry optimizations and the vibrational-frequencies calculations were performed using Gaussian 16 [44], while the electronic properties of the ground state and the excited states were calculated using Q-Chem [45]. The calculated gas-phase vibronic transition energies were corrected in order to match the 0–0 transition with the experimental gas-phase value. This resulted in a shift in the vibronic transitions associated with the excitation to L_b of -0.32 eV (arising from the difference between the reported gas-state experimental value of the 0–0 transition of 4.37 eV [8] and our calculated unperturbed value of 4.69 eV provided by CCSD/6-311+G(d) calculations) and a shift by -0.57 eV for the vibronic transitions associated with the excitation to L_a (given by the reported gas-state experimental value of the 0–0 transition of 4.54 eV [8] and our calculated unperturbed value of 5.11 eV). Finally, the value of σ used to construct the spectra (0.0004 frequency atomic units corresponding to 0.068 eV) was obtained by tuning the value estimated for Pyrene (about 0.02 eV) in a previous work [23] in order to optimize the spectral lineshape. The Pyrene value was evaluated by calculating the variance in the electronic transition energies of the semi-rigid chromophore in gas phase for several configurations within its MD conformational basin (harmonic-like basin).

NVT MD simulations of indole and 949 TIP3P water molecules were carried out in a cubic box of side 3.02356 nm using periodic boundary conditions, at 300 K. The size of the box was chosen in order to reproduce the experimental density of the system [46]. CHARMM36 [47,48] was used as the force field and the canonical sampling was achieved using the velocity rescaling thermostat [49]. Indole was considered in the ground or in one of the spectroscopically active (unperturbed) electronic excited states (the L_a and L_b excited states) by replacing the values of its atomic charges in the force field with the ESP charges [50,51] calculated at the EOM-CCSD/6-311+G(d) level. For each system simulation, the MD trajectory was carried out for 400 ns with a 2 fs timestep, which resulted in $20,000$ frames (taken each 20 ps) to be used in the MD-PMM procedure. The MD simulations were performed using Gromacs 2020.1 [52].

3.2. Results

Indole (see Figure 1) is a semi-rigid molecule, thus allowing us to consider a single conformational (quasi-harmonic) basin to fully describe its spectroscopic behavior. According to the model described in the theory section, we used as the reference structure for each perturbed electronic eigenstate of interest the energy minimum of the unperturbed electronic eigenstate best corresponding to the perturbed one, hence providing all the unperturbed electronic properties and vibrational modes and frequencies to be used. In Figure 2, we show the matrices given by the squared inner products of the mass-weighted Hessian eigenvectors (the squared elements of the Duschinsky matrix), as obtained for the unperturbed QC at the energy minima of the ground and L_b (panel A), or the ground, and L_a (panel B), the electronic, states. From the figure, it is clear that such matrices are nearly diagonal, well matching the requirement for the use of our simplified treatment of the vibronic transitions (note that, in both matrices, modes with the same index always have nearly identical frequencies).

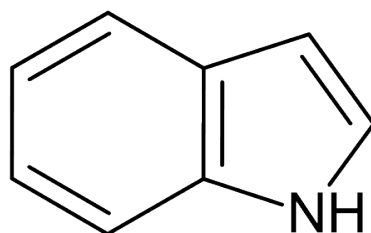


Figure 1. Indole structure.

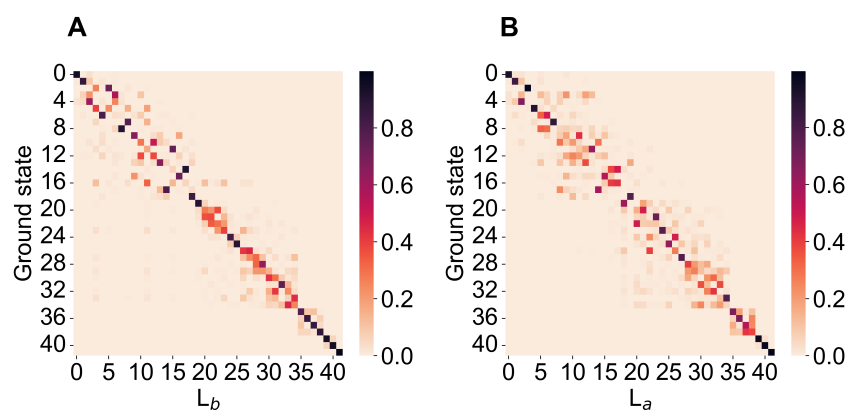


Figure 2. Matrices obtained by the squared elements of the Duschinsky matrix associated to the ground-to- L_b -state transition (A) and to the ground-to- L_a -state transition (B). Note that, in both matrices, modes with the same index always have nearly identical frequencies.

Concerning the modeling of the absorption spectrum, we obtained the ground-state ensemble by performing a long equilibrium MD simulation (400 ns) with the indole force-field parameters corresponding to the QC unperturbed electronic ground-state charge distribution (as usual, the QC perturbed electronic ground state is virtually identical to the unperturbed one, data not shown). From the obtained ground-state MD ensemble, via PMM, we reconstructed the corresponding distributions of the projections (Hermitian products) of the first and second perturbed electronic excited states on the unperturbed electronic states [25] (the ground state GS, the excited states L_b , L_a and the dark state $\pi\sigma^*$), obtained at the (unperturbed) ground-state optimized geometry (ground-state geometry). From such distributions, shown in Figures 3 and 4, it is evident that within the ground-state MD ensemble the perturbed first electronic excited state mostly corresponds to the L_b electronic state, while the perturbed second electronic excited state is largely corresponding to the L_a electronic state (see panels A). Interestingly, from the panel B of the same figures, we can realize that both perturbed electronic excited states essentially fluctuate between the L_a and L_b states, being nearly identical to only one of them at each MD frame (we disregard the few MD frames with the perturbed second electronic excited state projecting onto the dark state $\pi\sigma^*$).

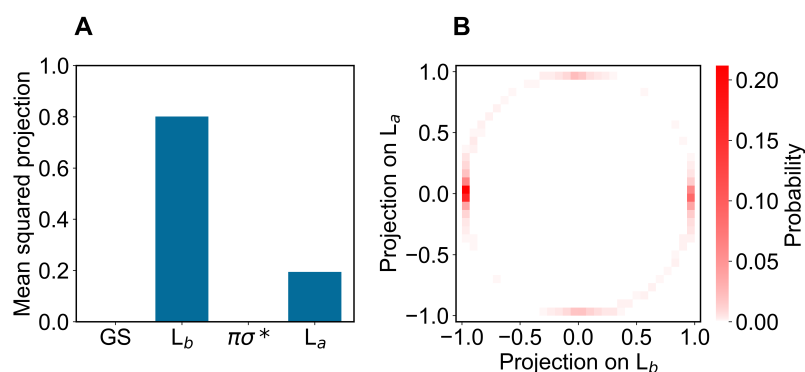


Figure 3. (A): Mean-squared projections of the perturbed first electronic excited state of indole, on the first four unperturbed electronic eigenstates (the ground state GS, the excited states L_b , L_a and the dark state $\pi\sigma^*$, in the figure ordered according to increasing energy) as obtained at the (unperturbed) ground-state geometry by the ground-state MD ensemble. (B): Probability distribution of the pair values of the projections of the perturbed first electronic excited state of indole, on the L_b and L_a states as obtained at the (unperturbed) ground-state geometry by the ground-state MD ensemble.

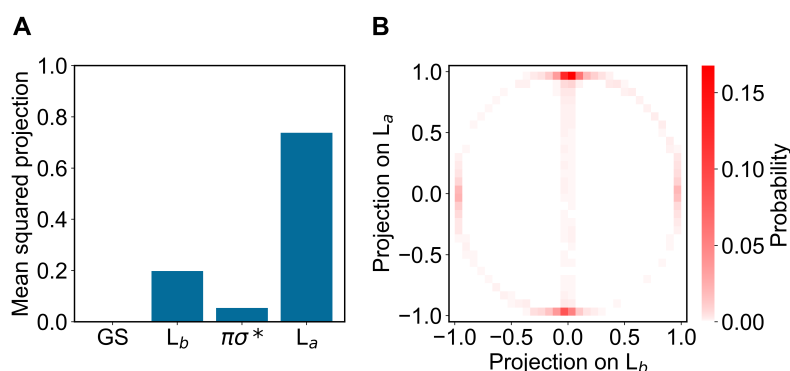


Figure 4. (A): Mean-squared projections of the perturbed second electronic excited state of indole, on the first four unperturbed electronic eigenstates (the ground state GS, the excited states L_b , L_a and the dark state $\pi\sigma^*$, in the figure ordered according to increasing energy) as obtained at the (unperturbed) ground-state geometry by the ground-state MD ensemble. (B): Probability distribution of the pair values of the projections of the perturbed second electronic excited state of indole, on the L_b and L_a states as obtained at the (unperturbed) ground-state geometry by the ground-state MD ensemble.

In order to obtain the absorption spectrum (including the vibronic details), we extracted from the ground-state MD simulation, for each of the first two perturbed electronic excited states, the MD frames where the perturbed electronic excited state of interest (as obtained at the ground-state geometry) is virtually identical either to the L_b or to the L_a state, thus allowing us to reconstruct (see the theory section) the corresponding vibronic spectra (for each MD frame we assumed the same electronic-state assignment over the whole relevant range of the mode coordinates). The complete absorption spectrum as shown in Figure 5 was obtained from the weighted summation of all the contributions (including the vibronic details) due to both the excited states. In this figure, we compare the experimental absorption spectrum with the calculated ones, as obtained according to the theory section using either our vibronic treatment or the vibronic structure provided by the algorithms implemented in Gaussian [37] (Gaussian vibronic treatment). Note that, due to the limited number of vibronic transitions considered by the Gaussian vibronic treatment, in order to mimic in the corresponding spectral signal the effect of the missing vibronic transitions, we scaled the estimated squared vibrational-state overlaps (as provided by Gaussian via the unperturbed absorption intensities) to normalize their sum (see Equation (14)): we assume all the missing vibronic transitions as included within the absorption range of interest and distributed to provide the same intensity relative increment for each vibronic transition considered. Therefore, the vibronic spectrum based on the Gaussian vibronic treatment reported should be considered as corresponding to the highest possible absorption intensity: i.e., the intensity of the spectrum we would obtain including within the Gaussian vibronic treatment all the relevant vibronic transitions, with, hence, no normalization scaling of the squared vibrational state overlaps, is likely to be lower. From the figure, it is clear the higher accuracy of our vibronic treatment in reproducing the details of the spectrum, although the Gaussian vibronic treatment also provides a proper spectrum intensity and width (both calculated spectra properly reproduce the position of the maximum). It is worth noting that due to computational limitations we always had to employ DFT calculations for evaluating the mass-weighted Hessian at the reference structures (electronic-energy minima) used to obtain the vibronic structure for the first two electronic transitions (the energy minima of the GS, L_a and L_b unperturbed electronic eigenstates). Therefore, the use of the vibronic treatment implemented in Gaussian, requiring full-space minima, forced us to also employ DFT calculations to obtain the optimized structures to be used for the Hessian calculations (for the PMM calculations we always used the higher level CCSD and EOM-CCSD methods). Conversely, when using our (simplified) vibronic treatment, requiring a minimum only within the quantum-mode subspace, we were able to utilize

DFT Hessian calculations for reference structures optimized at CCSD and EOM-CCSD level, thus possibly guaranteeing a higher accuracy. In addition, our approach allowed us to include a huge number of vibronic transitions (over a million transitions instead of about 100, as used within the Gaussian vibronic treatment) providing a virtually complete reconstruction of the vibronic structure for each electronic excitation. The results reported in Figure 5, indicating that the approximations we used to simplify the vibronic structure calculations are accurate, plainly show that the inclusion of a very large number of vibronic transitions and the possibility to treat separately the quantum- and classical-mode subspaces can provide a significant improvement in modeling vibronic spectra.

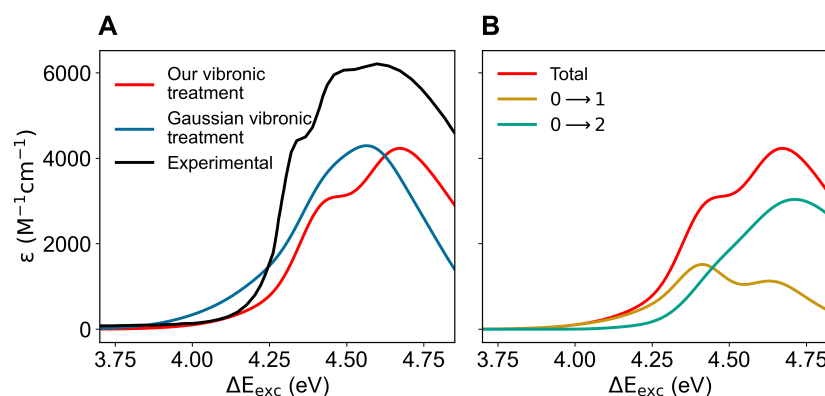


Figure 5. (A): Calculated (colored) and measured (black; adapted from Hilaire et al. [53]) absorption spectra of indole in aqueous solution. The predicted spectra were obtained using our vibronic treatment (red) and with the vibronic structure calculated using the algorithms implemented in Gaussian (blue), both as provided by the ground-state MD ensemble. (B): Calculated total absorption spectrum (using our vibronic treatment) of indole in aqueous solution and the corresponding contributions to the vibronic spectrum due to the first two electronic transitions.

In modeling the emission process, we had to consider the proper excited-state MD ensemble to be used for reconstructing the fluorescence spectrum due to the first excited-state radiative relaxation (as usual, we assumed no other radiative relaxations as a consequence of the much faster non-radiative transitions from higher excited states to the first excited state). From the absorption data discussed above, we know that the first two perturbed electronic excited states can be conceived as fluctuating between the L_a and L_b states, thus suggesting that the emission process should be modeled using the corresponding excited-state MD ensembles and geometries, i.e., using the corresponding excited-state MD force field and optimized geometry (L_a and L_b geometries). Note that as the fluorescence mean lifetime is much longer than the ones of the inter-conversion processes involving the first three perturbed excited states (within the GS geometry and MD ensemble, basically corresponding to the L_b , L_a and $\pi\sigma^*$ unperturbed states, respectively), we cannot assume the L_b ensemble as the proper excited-state MD ensemble to be used. Therefore, we used two different excited-state MD ensembles and geometries, using the L_b and L_a optimized geometries and corresponding MD simulations (we disregarded the spectroscopically inactive dark state). In order to verify the consistency of the MD ensembles obtained, we evaluated the mean-squared projections (mean-squared Hermitian products) of the perturbed electronic first excited state over the first four unperturbed electronic states (the ground state GS, the excited states L_b , L_a and the dark state $\pi\sigma^*$), as obtained either at the L_b or L_a geometry and MD ensemble (see panels A of Figures 6 and 7). From these figures, it is evident that within the L_b geometry and MD ensemble the perturbed first electronic state is coinciding with the L_b state, while within the L_a geometry and MD ensemble the same perturbed eigenstate is largely corresponding to the L_a state, although still projecting onto the L_b state. Interestingly, from panel B of Figure 7 it emerges that in this last case the perturbed first electronic excited state is not fluctuating between the L_a and L_b states but it is, rather, a stationary combination of them. These results indicate that we can use in both

cases the complete MD simulation to obtain a consistent excited-state MD ensemble for evaluating the emission spectrum (for the L_a -state MD ensemble considering the $\approx 80\%$ projection of the perturbed first excited state onto the L_a state).

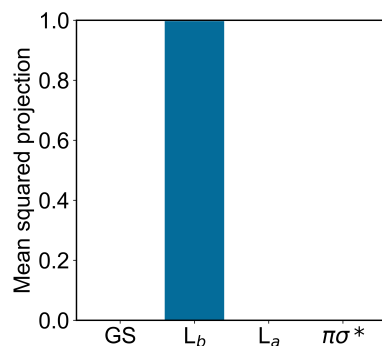


Figure 6. Mean-squared projections of the perturbed first electronic excited state of indole, on the first four unperturbed electronic eigenstates (the ground state GS, the excited states L_b , L_a and the dark state $\pi\sigma^*$, in the figure ordered according to increasing energy) as obtained at the L_b geometry by the L_b -state MD ensemble.

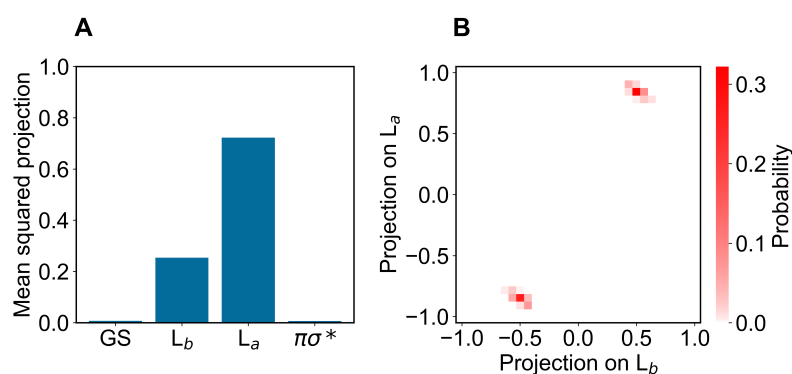


Figure 7. (A): Mean-squared projections of the perturbed first electronic excited state of indole, on the first four unperturbed electronic eigenstates (the ground state GS, the excited states L_b , L_a and the dark state $\pi\sigma^*$, in the figure ordered according to increasing energy) as obtained at the L_a geometry by the L_a state MD ensemble. (B): Probability distribution of the pair values of the projections of the perturbed first electronic excited state of indole, on the L_b and L_a states as obtained at the L_a geometry by the L_a -state MD ensemble.

Finally, in Figure 8 we show the comparison between the calculated emission spectra, as obtained employing either our vibronic treatment or the Gaussian vibronic treatment, with the experimental emission spectrum for the L_a (panel A) and L_b (panel B) excited-state geometries and MD ensembles. From this figure, it is evident that only the L_a geometry and MD ensemble reproduce the experimental signal, with a clear improvement in reproducing the spectrum when using our vibronic treatment. The comparison of such results with those obtained for the absorption process shows that after the excitation process, a fast relaxation must occur, providing a dramatic change in the perturbed first electronic excited-state population from being largely coinciding with the L_b state (see Figure 3) to largely resembling the L_a state.

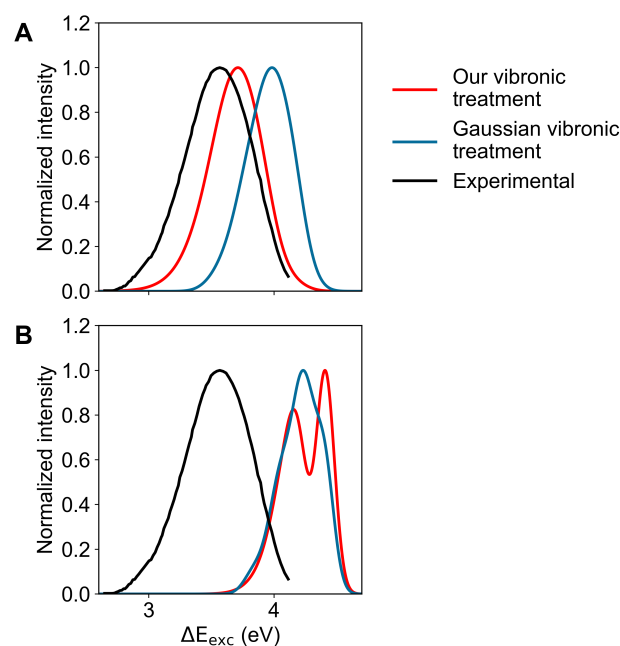


Figure 8. Calculated (coloured) and measured (black; adapted from Hilaire et al. [53]) normalized emission spectra of indole in aqueous solution. Spectra calculated using our vibronic treatment are reported in red, while the spectra obtained by the vibronic structure calculated using the algorithms implemented in Gaussian are reported in blue. (A): Spectra calculated in the L_a -state MD ensemble. (B): Spectra calculated in the L_b -state MD ensemble.

4. Conclusions

The use of general and typically accurate approximations for modelling vibronic transitions (see the Theory section), allowed us to relevantly simplify the vibronic treatment [16,17], resulting in a very efficient and accurate reconstruction of the absorption and emission spectra, within the MD-PMM framework. In fact, taking advantage of the approximately identical vibrational modes and frequencies of the energy minima involved in the electronic transitions, we are able to explicitly include in our treatment a huge number of vibronic transitions, which are necessary to reproduce the details of the spectral signal. Moreover, stemming from the approximations/simplifications adopted, we can easily discriminate between classical-like and quantum-mode vibronic transitions, allowing us to uncouple the corresponding vibronic calculations, hence permitting the use of the quantum-mode transitions only and avoiding the restriction of using ground and excited reference structures strictly corresponding to full-space energy minima, i.e., we need only the quantum coordinates to be properly energy minimized. Such a feature of the method allows the use of high-level calculations for the evaluation of properly minimized reference configurations and related fully reliable properties (e.g., by means of EOM-CCSD), still calculating the corresponding harmonic vibrational modes and frequencies via a less accurate but computationally much more affordable method (e.g., TD-DFT), often unable to provide the correct minimum energy position for the classical-like modes. The application of such an approach to aqueous Indole quantitatively reproduces both the experimental absorption and emission spectra with higher accuracy than the one obtained by employing the usual vibronic treatment as implemented in Gaussian [16,37]. Moreover, it also provided indications on indole-complex excited-state behavior, shedding light on the different sub-populations accessed by means of the absorption process, i.e., the L_a , L_b and $\pi\sigma^*$ (unperturbed) state sub-populations of the perturbed first and second electronic excited states. Finally, the comparison of the calculated emission spectra as obtained by the first (perturbed) excited-state MD ensemble and geometry corresponding to either the L_a or the L_b states clearly showed that, although the excitation provides a first perturbed excited state largely corresponding to the L_b state, in the emission, the L_a ensemble and geometry

can only provide a proper spectral signal, thus showing that a fast relevant relaxation of the electronic perturbed first excited-state population (converting the L_b sub-population into the L_a one) must occur.

Supplementary Materials: The following supporting information can be downloaded at: <https://www.mdpi.com/article/10.3390/molecules27238135/s1>, Figure S1: Vibronic spectrum of gas-phase indole calculated with different DFT functionals; Table S1: Electronic properties of gas-phase indole calculated with different DFT functionals. References [16,37–44] are cited in Supplementary Materials.

Author Contributions: Conceptualization, A.A. and M.D.; methodology, A.A.; software, C.G.C. and M.A.; validation, C.G.C., M.A., A.A. and M.D.; formal analysis, C.G.C., M.A., A.A. and M.D.; investigation, C.G.C.; writing—original draft preparation, C.G.C., M.A., A.A. and M.D.; writing—review and editing, C.G.C., M.A., A.A. and M.D.; visualization, C.G.C.; supervision, A.A. and M.D.; project administration, A.A. and M.D. All authors have read and agreed to the published version of the manuscript.

Funding: This work was partially funded by Sapienza University of Rome (progetti di Ateneo 2018/2019).

Data Availability Statement: The data presented in this study are available on request from the corresponding author.

Acknowledgments: The authors thank NVidia and CINECA for the computational support.

Conflicts of Interest: The authors declare no conflict of interest.

Appendix A

In this appendix, we show that when the nuclear coordinates of a molecule or a tightly bound molecular cluster, they can be subdivided into semi-classical and quantum degrees of freedom; within proper conditions (typically present in usual physical–chemical systems), we can locally (i.e., within each harmonic-like basin) express them via two different sets of the normal modes as obtained by the quantum coordinates' local minimum energy mass-weighted Hessian.

Let us assume that we can define the generalized nuclear coordinates as $q = \{\zeta, \alpha\}$, where ζ are semi-classical coordinates and α are quantum degrees of freedom, with no mixing between the semi-classical and quantum sub-spaces (i.e., within the whole accessible configurational space, the same definition of such coordinates can be used). Making use of the typical stiffness of the nuclear quantum coordinates providing at each semi-classical position ζ only tiny harmonic-like vibrations of the quantum coordinates around their local energy minimum $\alpha_0(\zeta)$, we can employ a theorem from analytical mechanics stating that the generalized coordinates can always be defined in such a way the mass tensor (the symmetric matrix \tilde{M}_q) becomes a block diagonal matrix [54]

$$\tilde{M}_q \cong \begin{bmatrix} \tilde{M}_{\zeta,\zeta} & \tilde{0} \\ \tilde{0} & \tilde{M}_{\alpha,\alpha} \end{bmatrix} \quad (\text{A1})$$

where the symmetric, typically virtually constant within a harmonic-like basin, matrices $\tilde{M}_{\zeta,\zeta}$, $\tilde{M}_{\alpha,\alpha}$ are the mass tensor (diagonal) blocks corresponding to the semi-classical and quantum degrees of freedom, respectively (the approximation becoming exact on the $\alpha_0(\zeta)$ surface), with, then, the kinetic energy operator \hat{K} (expressed within the coordinate representation) given by the sum of two independent terms (concerning the momenta)

$$\hat{K} \cong K_\zeta + \hat{K}_\alpha \quad (\text{A2})$$

with K_ζ identical to the classical kinetic energy of the semi-classical degrees of freedom (i.e., involving only the classical coordinates conjugated momenta π_ζ) and \hat{K}_α providing the kinetic energy operator of the quantum degrees of freedom (i.e., involving only the operators of the quantum coordinate conjugated momenta $\hat{\pi}_\alpha$). Note that such a

semi-classical and quantum-momenta uncoupling becomes exact only over the $\alpha_0(\zeta)$ surface. However, given the tiny displacements allowed for the quantum coordinates around each α_0 position, Equation (A2) can be used as a general accurate approximation. Therefore, we can readily obtain the vibrational Hamiltonian operator at each semi-classical configuration via

$$\begin{aligned}\hat{H}_v &= \hat{K}_\alpha + \mathcal{U}_e(\zeta, \alpha) - \mathcal{U}_e(\zeta, \alpha_0(\zeta)) \\ &\cong \hat{K}_\alpha + \Delta\alpha^T \frac{\tilde{G}_{\alpha,\alpha}}{2} \Delta\alpha\end{aligned}\quad (\text{A3})$$

$$\Delta\alpha = \alpha - \alpha_0(\zeta) \quad (\text{A4})$$

$$\hat{K}_\alpha = \hat{\pi}_\alpha^T \frac{(\tilde{M}_{\alpha,\alpha})^{-1}}{2} \hat{\pi}_\alpha \quad (\text{A5})$$

$$[\tilde{G}_{\alpha,\alpha}]_{i,j} = \frac{\partial^2 \mathcal{U}_e}{\partial \alpha_i \partial \alpha_j} \quad (\text{A6})$$

where \mathcal{U}_e is the electronic energy and $\tilde{G}_{\alpha,\alpha}$ is the Hessian matrix (within the α subspace) of the electronic energy, as obtained at $\zeta, \alpha_0(\zeta)$. Introducing the quantum-mass weighted coordinates $\Delta\alpha' = \sqrt{\tilde{M}_{\alpha,\alpha}} \Delta\alpha$ with conjugated momenta operators $\hat{\pi}_{\alpha'} = \left(\sqrt{\tilde{M}_{\alpha,\alpha}}\right)^{-1} \hat{\pi}_\alpha = \sqrt{(\tilde{M}_{\alpha,\alpha})^{-1}} \hat{\pi}_\alpha$, we obtain (expressing $\Delta\alpha$ and $\hat{\pi}_\alpha$ via $\Delta\alpha'$ and $\hat{\pi}_{\alpha'}$)

$$\hat{H}_v \cong \frac{1}{2} \hat{\pi}_{\alpha'}^T \hat{\pi}_{\alpha'} + (\Delta\alpha')^T \sqrt{(\tilde{M}_{\alpha,\alpha})^{-1}} \frac{\tilde{G}_{\alpha,\alpha}}{2} \sqrt{(\tilde{M}_{\alpha,\alpha})^{-1}} \Delta\alpha' \quad (\text{A7})$$

where $\sqrt{(\tilde{M}_{\alpha,\alpha})^{-1}} \tilde{G}_{\alpha,\alpha} \sqrt{(\tilde{M}_{\alpha,\alpha})^{-1}}$ is the mass-weighted Hessian, within the harmonic-like basin independent of the $\zeta, \alpha_0(\zeta)$ configuration and often invariant over the different accessible basins, with eigenvectors and eigenvalues providing the (quantum) vibrational modes and frequencies. Note that due to the symmetry of the $\tilde{M}_{\alpha,\alpha}$ matrix, it follows that

$$\sqrt{\tilde{M}_{\alpha,\alpha}} = \left(\sqrt{\tilde{M}_{\alpha,\alpha}}\right)^T = \sqrt{(\tilde{M}_{\alpha,\alpha})^T} \quad (\text{A8})$$

$$\sqrt{(\tilde{M}_{\alpha,\alpha})^{-1}} = \left(\sqrt{(\tilde{M}_{\alpha,\alpha})^{-1}}\right)^T = \sqrt{\left((\tilde{M}_{\alpha,\alpha})^{-1}\right)^T} \quad (\text{A9})$$

Let us consider now the Hessian \tilde{G}_q within the whole $q = \{\zeta, \alpha\}$ space

$$[\tilde{G}_q]_{i,j} = \frac{\partial^2 \mathcal{U}_e}{\partial q_i \partial q_j} \quad (\text{A10})$$

as obtained at $\zeta, \alpha_0(\zeta)$ with ζ not far from the local minimum energy position ζ_0 : i.e., the Hessian is obtained within the harmonic-like basin corresponding to the full-space minimum-energy position $\zeta_0, \alpha_0(\zeta_0)$. It is worth noting that due to the very different stiffness of the quantum and semi-classical coordinates, when considering positions not far from $\zeta_0, \alpha_0(\zeta_0)$, we typically have $\partial^2 \mathcal{U}_e / \partial \zeta_l \partial \alpha_n \approx 0$, thus providing

$$\tilde{G}_q \approx \begin{bmatrix} \tilde{G}_{\zeta,\zeta} & \tilde{0} \\ \tilde{0} & \tilde{G}_{\alpha,\alpha} \end{bmatrix} \quad (\text{A11})$$

Moreover, in general, when expressing the elements of \tilde{G}_q via the Cartesian coordinates of the laboratory reference frame \mathbf{x} , we obtain

$$\begin{aligned} [\tilde{G}_q]_{i,j} &= \sum_l \sum_{l'} \frac{\partial^2 \mathcal{U}_e}{\partial x_{l'} \partial x_l} \frac{\partial x_{l'}}{\partial q_i} \frac{\partial x_l}{\partial q_j} + \sum_l \frac{\partial \mathcal{U}_e}{\partial x_l} \frac{\partial^2 x_l}{\partial q_i \partial q_j} \\ &= \sum_l \sum_{l'} [\tilde{G}_x]_{l,l'} [\tilde{T}]_{l',i} [\tilde{T}]_{l,j} + \sum_l \frac{\partial \mathcal{U}_e}{\partial x_l} \frac{\partial^2 x_l}{\partial q_i \partial q_j} \end{aligned} \quad (\text{A12})$$

with $[\tilde{G}_x]_{l,l'} = \partial^2 \mathcal{U}_e / \partial x_{l'} \partial x_l$ the elements of the Cartesian Hessian and

$$[\tilde{T}]_{l',i} = \frac{\partial x_{l'}}{\partial q_i} \quad (\text{A13})$$

$$[\tilde{T}]_{l,j} = \frac{\partial x_l}{\partial q_j} \quad (\text{A14})$$

the elements of the transformation matrix \tilde{T} defined by

$$d\mathbf{x} = \tilde{T} d\mathbf{q} \quad (\text{A15})$$

and involved in the mass tensor transformation

$$\tilde{M}_q = \tilde{T}^T \tilde{M}_x \tilde{T} \quad (\text{A16})$$

where \tilde{M}_x is the (diagonal) Cartesian mass tensor with elements $[\tilde{M}_q]_{l,l'} = m_l \delta_{l,l'}$ given by the particle masses m_l (note that the index l runs over all the Cartesian coordinates of the particles and, thus, m_l has a three-fold degeneration). From Equations (A12)–(A14), we then have

$$[\tilde{G}_q]_{i,j} = [\tilde{T}^T \tilde{G}_x \tilde{T}]_{i,j} + \sum_l \frac{\partial \mathcal{U}_e}{\partial x_l} \frac{\partial^2 x_l}{\partial q_i \partial q_j} \quad (\text{A17})$$

plainly showing that only when evaluating the Hessian at a full-space energy minimum (i.e., $\partial \mathcal{U}_e / \partial x_l = 0$) or when dealing with a linear coordinate transformation (i.e., constant \tilde{T} matrix and, thus, $\partial^2 x_l / \partial q_i \partial q_j = 0$), we exactly have that the \mathbf{q} space Hessian is obtained by simply transforming the Cartesian Hessian via the same transformation used to obtain \tilde{M}_q from \tilde{M}_x . However, considering that within each harmonic-like basin the semi-classical coordinates are not far from their minimum-energy position, with the Hessian always obtained at fully energy minimized quantum coordinates (i.e., $\partial \mathcal{U}_e / \partial x_l \approx 0$), and the transformation matrix \tilde{T} able to be treated as almost constant, we can write

$$\tilde{G}_q \approx \tilde{T}^T \tilde{G}_x \tilde{T} \quad (\text{A18})$$

typically valid for each $\zeta, \alpha_0(\zeta)$ configuration within the harmonic-like basin. From Equations (A1) and (A11), we can obtain the \mathbf{q} full-space mass-weighted Hessian

$$\begin{aligned}
& \sqrt{(\tilde{M}_q)^{-1}} \tilde{G}_q \sqrt{(\tilde{M}_q)^{-1}} \\
\approx & \begin{bmatrix} \sqrt{(\tilde{M}_{\zeta,\zeta})^{-1}} & \tilde{0} \\ \tilde{0} & \sqrt{(\tilde{M}_{\alpha,\alpha})^{-1}} \end{bmatrix} \begin{bmatrix} \tilde{G}_{\zeta,\zeta} & \tilde{0} \\ \tilde{0} & \tilde{G}_{\alpha,\alpha} \end{bmatrix} \begin{bmatrix} \sqrt{(\tilde{M}_{\zeta,\zeta})^{-1}} & \tilde{0} \\ \tilde{0} & \sqrt{(\tilde{M}_{\alpha,\alpha})^{-1}} \end{bmatrix} \\
= & \begin{bmatrix} \sqrt{(\tilde{M}_{\zeta,\zeta})^{-1}} \tilde{G}_{\zeta,\zeta} \sqrt{(\tilde{M}_{\zeta,\zeta})^{-1}} & \tilde{0} \\ \tilde{0} & \sqrt{(\tilde{M}_{\alpha,\alpha})^{-1}} \tilde{G}_{\alpha,\alpha} \sqrt{(\tilde{M}_{\alpha,\alpha})^{-1}} \end{bmatrix}
\end{aligned} \tag{A19}$$

clearly showing that the eigenvectors of such a mass-weighted Hessian (i.e., the vibrational modes) correspond to two independent groups: the classical-like modes as provided by the block of the semi-classical coordinates and the quantum modes as provided by the quantum-coordinate block. Note again that within the harmonic-like basin, at least the quantum coordinate block and, hence, its eigenvectors and eigenvalues, are independent of the configuration used to evaluate the mass-weighted Hessian (the semi-classical coordinates, possibly involving anharmonic effects, may provide a slightly different configuration-dependent mass-weighted Hessian block). Finally, from Equations (A16) and (A18), we also have

$$\begin{aligned}
& \sqrt{(\tilde{M}_q)^{-1}} \tilde{G}_q \sqrt{(\tilde{M}_q)^{-1}} = \sqrt{\tilde{M}_q} (\tilde{M}_q)^{-1} \tilde{G}_q \sqrt{(\tilde{M}_q)^{-1}} \\
\approx & \sqrt{\tilde{M}_q} \tilde{T}^{-1} (\tilde{M}_x)^{-1} (\tilde{T}^T)^{-1} \tilde{T}^T \tilde{G}_x \tilde{T} \sqrt{(\tilde{M}_q)^{-1}} \\
= & \sqrt{\tilde{M}_q} \tilde{T}^{-1} \sqrt{(\tilde{M}_x)^{-1}} \sqrt{(\tilde{M}_x)^{-1}} \tilde{G}_x \sqrt{(\tilde{M}_x)^{-1}} \sqrt{\tilde{M}_x} \tilde{T} \sqrt{(\tilde{M}_q)^{-1}} \\
= & \tilde{\Theta}^{-1} \sqrt{(\tilde{M}_x)^{-1}} \tilde{G}_x \sqrt{(\tilde{M}_x)^{-1}} \tilde{\Theta}
\end{aligned} \tag{A20}$$

with

$$\tilde{\Theta} = \sqrt{\tilde{M}_x} \tilde{T} \sqrt{(\tilde{M}_q)^{-1}} \tag{A21}$$

the matrix for the $\sqrt{\tilde{M}_q} \mathbf{q} \rightarrow \sqrt{\tilde{M}_x} \mathbf{x}$ coordinate transformation (note that according to the approximations used, such a transformation matrix is also virtually constant within the harmonic-like basin). Equation (A21) demonstrates that within the approximations used, for a given $\zeta, \alpha_0(\zeta)$ configuration, the eigenvectors and eigenvalues of the Cartesian mass-weighted Hessian $\sqrt{(\tilde{M}_x)^{-1}} \tilde{G}_x \sqrt{(\tilde{M}_x)^{-1}}$ correspond to the ones obtained by the generalized coordinate mass-weighted Hessian $\sqrt{(\tilde{M}_q)^{-1}} \tilde{G}_q \sqrt{(\tilde{M}_q)^{-1}}$, thus providing the proper classical-like and quantum vibrational modes, with the latter and their frequencies representative of the whole harmonic-like basin: the quantum modes provided by the quantum-coordinate mass-weighted Hessian and the transformation matrix $\tilde{\Theta}$ for expressing them within the Cartesian mass-weighted coordinate basis set, are both virtually constant. Therefore, regardless of the semi-classical configuration chosen, we always consider all the eigenvectors of the Cartesian mass-weighted Hessian with frequencies ν such that $h\nu > k_B T$ as corresponding to the eigenvectors of the quantum-coordinate mass-weighted Hessian $\sqrt{(\tilde{M}_{\alpha,\alpha})^{-1}} \tilde{G}_{\alpha,\alpha} \sqrt{(\tilde{M}_{\alpha,\alpha})^{-1}}$, thus providing the quantum vibrational modes and frequencies of at least the selected harmonic-like basin, see Equation (A7) (h is the Planck constant, k_B is the Boltzmann constant and T is the absolute temperature).

References

1. Eftink, M. Fluorescence techniques for studying protein structure. *Methods Biochem. Anal.* **1991**, *35*, 127–205. [[PubMed](#)]
2. Beechem, J.; Brand, L. Time-resolved fluorescence of proteins. *Annu. Rev. Biochem.* **1985**, *54*, 43–71. [[CrossRef](#)] [[PubMed](#)]
3. Lakowicz, J.R. *Principles of Fluorescence Spectroscopy*; Springer: New York, NY, USA, 2006.
4. Kister, A.E. *Protein Supersecondary Structures*, 2nd ed.; Humana: New York, NY, USA, 2019.
5. Burstein, E.; Vedenkina, N.; Ivkova, M. Fluorescence and the location of tryptophan residues in protein molecules. *Photochem. Photobiol.* **1973**, *18*, 263–279. [[CrossRef](#)] [[PubMed](#)]
6. Reshetnyak, Y.K.; Burstein, E.A. Decomposition of Protein Tryptophan Fluorescence Spectra into Log-Normal Components. II. The Statistical Proof of Discreteness of Tryptophan Classes in Proteins. *Biophys. J.* **2001**, *81*, 1710–1734. [[CrossRef](#)] [[PubMed](#)]
7. Callis, P.R.; Vivian, J.T.; Slater, L.S. Ab initio calculations of vibronic spectra for indole. *Chem. Phys. Lett.* **1995**, *244*, 53–58. [[CrossRef](#)]
8. Serrano-Andrés, L.; Roos, B.O. Theoretical Study of the Absorption and Emission Spectra of Indole in the Gas Phase and in a Solvent. *J. Am. Chem. Soc.* **1996**, *118*, 185–195. [[CrossRef](#)]
9. Serrano-Andrés, L.; Borin, A.C. A theoretical study of the emission spectra of indole and its analogs: Indene, benzimidazole, and 7-azaindole. *Chem. Phys.* **2000**, *262*, 267–283. [[CrossRef](#)]
10. Brand, C.; Küpper, J.; Pratt, D.W.; Meerts, W.L.; Krügler, D.; Tatchen, J.; Schmitt, M. Vibronic coupling in indole: I. Theoretical description of the 1La–1Lb interaction and the electronic spectrum. *Phys. Chem. Chem. Phys.* **2010**, *12*, 4968–4979. [[CrossRef](#)]
11. Giussani, A.; Merchán, M.; Roca-Sanjuán, D.; Lindh, R. Essential on the Photophysics and Photochemistry of the Indole Chromophore by Using a Totally Unconstrained Theoretical Approach. *J. Chem. Theory Comput.* **2011**, *7*, 4088–4096. [[CrossRef](#)]
12. Arulmozhiraja, S.; Coote, M.L. 1L a and 1L b states of indole and azaindole: Is density functional theory inadequate? *J. Chem. Theory Comput.* **2012**, *8*, 575–584. [[CrossRef](#)] [[PubMed](#)]
13. Brisker-Klaiman, D.; Dreuw, A. Explaining Level Inversion of the La and Lb States of Indole and Indole Derivatives in Polar Solvents. *ChemPhysChem* **2015**, *16*, 1695–1702. [[CrossRef](#)] [[PubMed](#)]
14. Abou-Hatab, S.; Matsika, S. Theoretical Investigation of Positional Substitution and Solvent Effects on n-Cyanoindole Fluorescent Probes. *J. Phys. Chem. B* **2019**, *123*, 7424–7435. [[CrossRef](#)] [[PubMed](#)]
15. Manian, A.; Shaw, R.A.; Lyskov, I.; Russo, S.P. The quantum chemical solvation of indole: Accounting for strong solute–solvent interactions using implicit/explicit models. *Phys. Chem. Chem. Phys.* **2022**, *24*, 3357–3369. [[CrossRef](#)] [[PubMed](#)]
16. Santoro, F.; Lami, A.; Improta, R.; Bloino, J.; Barone, V. Effective method for the computation of optical spectra of large molecules at finite temperature including the Duschinsky and Herzberg–Teller effect: The Qx band of porphyrin as a case study. *J. Chem. Phys.* **2008**, *128*, 224311. [[CrossRef](#)] [[PubMed](#)]
17. Cerezo, J.; Ferrer, F.J.A.; Prampolini, G.; Santoro, F. Adiabatic-Molecular Dynamics Generalized Vertical Hessian Approach: A Mixed Quantum Classical Method To Compute Electronic Spectra of Flexible Molecules in the Condensed Phase. *J. Chem. Theory Comput.* **2020**, *16*, 1215–1231. [[CrossRef](#)] [[PubMed](#)]
18. Mennucci, B.; Cappelli, C.; Guido, C.A.; Cammi, R.; Tomasi, J. Structures and Properties of Electronically Excited Chromophores in Solution from the Polarizable Continuum Model Coupled to the Time-Dependent Density Functional Theory. *J. Phys. Chem. A* **2009**, *113*, 3009–3020. [[CrossRef](#)]
19. Marenich, A.; Cramer, C.J.; Truhlar, D.G. Electronic Absorption Spectra and Solvatochromic Shifts by the Vertical Excitation Model: Solvated Clusters and Molecular Dynamics Sampling. *J. Phys. Chem. B* **2015**, *119*, 958–967. [[CrossRef](#)]
20. Zuehlsdorff, T.J.; Isborn, C.M. Modeling absorption spectra of molecules in solution. *Int. J. Quant. Chem.* **2019**, *119*, 25719. [[CrossRef](#)]
21. Eilmes, A. Effect of Molecular Vibrations on the MD/QC-Simulated Absorption Spectra. *Int. J. Quantum Chem.* **2014**, *114*, 261–270. [[CrossRef](#)]
22. Law, K.K.; Hassanali, A.A. The importance of nuclear quantum effects in spectral line broadening of optical spectra and electrostatic properties in aromatic chromophores. *J. Chem. Phys.* **2018**, *148*, 102331. [[CrossRef](#)]
23. D’Abramo, M.; Aschi, M.; Amadei, A. Theoretical modeling of UV-Vis absorption and emission spectra in liquid state systems including vibrational and conformational effects: Explicit treatment of the vibronic transitions. *J. Chem. Phys.* **2014**, *140*, 164104. [[CrossRef](#)] [[PubMed](#)]
24. Aschi, M.; Spezia, R.; Di Nola, A.; Amadei, A. A first-principles method to model perturbed electronic wavefunctions: The effect of an external homogeneous electric field. *Chem. Phys. Lett.* **2001**, *344*, 374–380. [[CrossRef](#)]
25. Amadei, A.; D’Alessandro, M.; D’Abramo, M.; Aschi, M. Theoretical characterization of electronic states in interacting chemical systems. *J. Chem. Phys.* **2009**, *130*, 084109. [[CrossRef](#)] [[PubMed](#)]
26. Zanetti-Polzi, L.; Del Galdo, S.; Daidone, I.; D’Abramo, M.; Barone, V.; Aschi, M.; Amadei, A. Extending the perturbed matrix method beyond the dipolar approximation: Comparison of different levels of theory. *Phys. Chem. Chem. Phys.* **2018**, *20*, 24369–24378. [[CrossRef](#)] [[PubMed](#)]
27. D’Alessandro, M.; Aschi, M.; Mazzuca, C.; Palleschi, A.; Amadei, A. Theoretical modeling of UV-Vis absorption and emission spectra in liquid state systems including vibrational and conformational effects: The vertical transition approximation. *J. Chem. Phys.* **2013**, *139*, 114102. [[CrossRef](#)] [[PubMed](#)]
28. Daidone, I.; Aschi, M.; Zanetti-Polzi, L.; Di Nola, A.; Amadei, A. On the origin of IR spectral changes upon protein folding. *Chem. Phys. Lett.* **2010**, *488*, 213–218. [[CrossRef](#)]

29. Amadei, A.; Daidone, I.; Zanetti-Polzi, L.; Aschi, M. Modeling quantum vibrational excitations in condensed-phase molecular systems. *Theor. Chem. Acc.* **2011**, *129*, 31–43. [[CrossRef](#)]
30. Chen, C.G.; Nardi, A.N.; Giustini, M.; D'Abramo, M. Absorption behavior of doxorubicin hydrochloride in visible region in different environments: A combined experimental and computational study. *Phys. Chem. Chem. Phys.* **2022**, *24*, 12027–12035. [[CrossRef](#)]
31. Amadei, A.; Daidone, I.; Aschi, M. A general theoretical model for electron transfer reactions in complex systems. *Phys. Chem. Chem. Phys.* **2012**, *14*, 1360–1370. [[CrossRef](#)] [[PubMed](#)]
32. Aschi, M.; D'Abramo, M.; Amadei, A. Photoinduced electron transfer in a dichromophoric peptide: A numerical experiment. *Theor. Chem. Acc.* **2016**, *135*, 132. [[CrossRef](#)]
33. Piacente, G.; Amadei, A.; D'Abramo, M.; Daidone, I.; Aschi, M. Theoretical-computational modeling of photo-induced charge separation spectra and charge recombination kinetics in solution. *Phys. Chem. Chem. Phys.* **2014**, *16*, 20624–20638. [[CrossRef](#)]
34. Zanetti-Polzi, L.; Aschi, M.; Amadei, A.; Daidone, I. Alternative Electron-Transfer Channels Ensure Ultrafast Deactivation of Light-Induced Excited States in Riboflavin Binding Protein. *J. Phys. Chem. Lett.* **2017**, *8*, 3321–3327. [[CrossRef](#)] [[PubMed](#)]
35. Aschi, M.; Barone, V.; Carlotti, B.; Daidone, I.; Elisei, F.; Amadei, A. Photoexcitation and relaxation kinetics of molecular systems in solution: Towards a complete in silico model. *Phys. Chem. Chem. Phys.* **2016**, *18*, 28919–28931. [[CrossRef](#)] [[PubMed](#)]
36. Del Galdo, S.; Aschi, M.; Amadei, A. IR spectroscopy of condensed phase systems: Can the environment induce vibrational mode coupling? *Chem. Phys. Lett.* **2021**, *763*, 138168. [[CrossRef](#)]
37. Barone, V.; Bloino, J.; Biczysko, M.; Santoro, F. Fully Integrated Approach to Compute Vibrationally Resolved Optical Spectra: From Small Molecules to Macrosystems. *J. Chem. Theory Comput.* **2009**, *5*, 540–554. [[CrossRef](#)]
38. Zhao, Y.; Truhlar, D.G. The M06 suite of density functionals for main group thermochemistry, thermochemical kinetics, noncovalent interactions, excited states, and transition elements: Two new functionals and systematic testing of four M06-class functionals and 12 other functionals. *Theor. Chem. Acc.* **2008**, *120*, 215–241. [[CrossRef](#)]
39. Kendall, R.A.; Dunning, T.H.; Harrison, R.J. Electron affinities of the first-row atoms revisited. Systematic basis sets and wave functions. *J. Chem. Phys.* **1992**, *96*, 6796–6806. [[CrossRef](#)]
40. Stephens, P.J.; Devlin, F.J.; Chabalowski, C.F.; Frisch, M.J. Ab Initio Calculation of Vibrational Absorption and Circular Dichroism Spectra Using Density Functional Force Fields. *J. Chem. Phys.* **1994**, *98*, 11623–11627. [[CrossRef](#)]
41. Yanai, T.; Tew, D.P.; Handy, N.C. A new hybrid exchange–correlation functional using the Coulomb-attenuating method (CAM-B3LYP). *Chem. Phys. Lett.* **2004**, *393*, 51–57. [[CrossRef](#)]
42. Adamo, C.; Barone, V. Toward reliable density functional methods without adjustable parameters: The PBE0 model. *J. Chem. Phys.* **1999**, *110*, 6158–6170. [[CrossRef](#)]
43. Chai, J.D.; Head-Gordon, M. Long-range corrected hybrid density functionals with damped atom–atom dispersion corrections. *Phys. Chem. Chem. Phys.* **2008**, *10*, 6615–6620. [[CrossRef](#)]
44. Frisch, M.J.; Trucks, G.W.; Schlegel, H.B.; Scuseria, G.E.; Robb, M.A.; Cheeseman, J.R.; Scalmani, G.; Barone, V.; Petersson, G.A.; Nakatsuji, H.; et al. *Gaussian-16 Revision B.01*; Gaussian Inc.: Wallingford, CT, USA, 2016.
45. Shao, Y.; Gan, Z.; Epifanovsky, E.; Gilbert, A.T.; Wormit, M.; Kussmann, J.; Lange, A.W.; Behn, A.; Deng, J.; Feng, X.; et al. Advances in molecular quantum chemistry contained in the Q-Chem 4 program package. *Mol. Phys.* **2015**, *113*, 184–215. [[CrossRef](#)]
46. Del Galdo, S.; Marracino, P.; D'Abramo, M.; Amadei, A. In silico characterization of protein partial molecular volumes and hydration shells. *Phys. Chem. Chem. Phys.* **2015**, *17*, 31270–31277. [[CrossRef](#)]
47. Vanommeslaeghe, K.; Hatcher, E.; Acharya, C.; Kundu, S.; Zhong, S.; Shim, J.; Darian, E.; Guvench, O.; Lopes, P.; Vorobyov, I.; et al. CHARMM general force field: A force field for drug-like molecules compatible with the CHARMM all-atom additive biological force fields. *J. Comp. Chem.* **2010**, *31*, 671–690. [[CrossRef](#)]
48. Best, R.B.; Zhu, X.; Shim, J.; Lopes, P.E.M.; Mittal, J.; Feig, M.; MacKerell, A.D. Optimization of the Additive CHARMM All-Atom Protein Force Field Targeting Improved Sampling of the Backbone ψ , ϕ and Side-Chain χ_1 and χ_2 Dihedral Angles. *J. Chem. Theory Comput.* **2012**, *8*, 3257–3273. [[CrossRef](#)] [[PubMed](#)]
49. Bussi, G.; Donadio, D.; Parrinello, M. Canonical sampling through velocity rescaling. *J. Chem. Phys.* **2007**, *126*, 014101. [[CrossRef](#)] [[PubMed](#)]
50. Singh, U.C.; Kollman, P.A. An approach to computing electrostatic charges for molecules. *J. Comp. Chem.* **1984**, *5*, 129–145. [[CrossRef](#)]
51. Besler, B.H.; Merz, K.M., Jr.; Kollman, P.A. Atomic charges derived from semiempirical methods. *J. Comp. Chem.* **1990**, *11*, 431–439. [[CrossRef](#)]
52. Abraham, M.J.; Murtola, T.; Schulz, R.; Páll, S.; Smith, J.C.; Hess, B.; Lindahl, E. GROMACS: High performance molecular simulations through multi-level parallelism from laptops to supercomputers. *SoftwareX* **2015**, *1-2*, 19–25. [[CrossRef](#)]
53. Hilaire, M.R.; Mukherjee, D.; Troxler, T.; Gai, F. Solvent dependence of cyanoindole fluorescence lifetime. *Chem. Phys. Lett.* **2017**, *685*, 133–138. [[CrossRef](#)] [[PubMed](#)]
54. Gallavotti, G. *Elements of Mechanics*; Springer: Berlin/Heidelberg, Germany, 1983.